Multiscale Modeling of Mixing Behavior in a 3D Atom Transfer Radical Copolymerization Stirred-Tank Reactor

Le Xie, Li-Tao Zhu, Zheng-Hong Luo,* Chong-Wen Jiang

Multiscale mixing phenomena in stirred-tank polymerization reactors are mainly caused by stir agitation, which performs a key function in macroscopic and microscopic flow fields. Both macroscopic and microscopic flow fields interact with each other and significantly affect the microstructure and product distribution of the resultant polymers. In this work, a computational fluid dynamics model combining the moment method used in the polymerization engineering field is implemented and validated using open data. Multiscale properties are characterized in terms of macroscopic mixing fields and the polymer microscopic structure of the atom transfer radical copolymerization system of methyl methacrylate and 2-(trimethylsilyl) ethyl methacrylate. Agitation in a 3D stirred tank is also thoroughly studied by using the multiple reference frame approach, and the effects of several important parameters, such as impeller speed, impeller types, and feeding position, on the macroscopic and microscopic flow fields are investigated on the basis of the validated model. Interdependent relationships among agitation, multiscale flow fields, and polymerization are described clearly. The results highlight the function of stirring and provide useful guidelines for the scale-up of stirred-tank polymerization reactors.

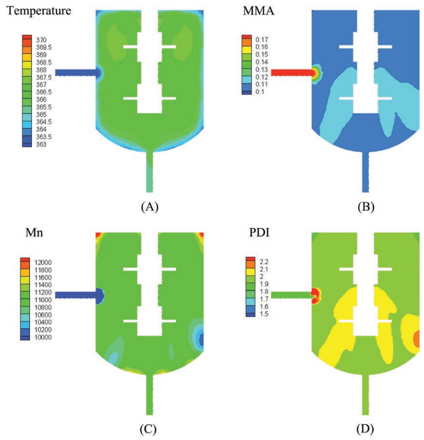

1. Introduction

The stirred tank reactor (STR) is one of the most commonly used industrial equipment for reaction, mixture, crystallization, and other unit operations.[1–3] Owing to the existence of different impeller, baffle, and other configurations, flow fields in STRs are usually more complicated than those in other reactors.[4,5] Improving flow fields in stirred reactors will benefit their optimization, scale-up, and the control of production capability, which is mainly related to mixing performance. High mixing efficiency is of considerable importance in stirred reactors. In general, the mixing performance of a reactor is responsible for both macroscale (e.g., temperature and concentration) and microscale (e.g., product molecular weight) fields. Both fields comprise multiscale properties that are prevalent in STRs and are mainly affected by stirring.

Experimental fluid dynamics (EFD) and computational fluid dynamics (CFD) are two common methods used to investigate flow fields in STRs.[6,7] EFD usually requires online measurement of the velocity, temperature, and concentration distributions through experimental techniques,

Dr. L. Xie, L.-T. Zhu, Prof. Z.-H. Luo
Department of Chemical Engineering
College of Chemistry and Chemical Engineering
Shanghai Jiao Tong University
Shanghai 200240, P. R. China
E-mail: luozh@sjtu.edu.cn
Prof. C.-W. Jiang
College of Chemistry and Chemical Engineering
Central South University
Changsha 410083, P. R. China

Macromol. React. Eng. **2016**, DOI: 10.1002/mren.201600022

such as laser Doppler anemometry and particle image velocimetry.[8–11] However, the measurement apparatus presents a variety of defects under specific operating conditions. Considering these limitations, available experimental data on EFD may be limited.[7] By comparison, CFD can capture detailed information on flow fields in reactors. The data obtained from this technique are highly beneficial for replacing the time-consuming and expensive experiments performed in the EFD technique to a certain extent.[5] CFD simulation can theoretically be carried out under any operating condition.

Over the past several decades, a number of CFD models have been proposed to describe hydrodynamic behavior in STRs. However, limited studies have investigated the multiscale properties of polymerization systems. These properties are strongly agitation-dependent. In polymerization systems, the behavior of stirred tanks is fairly complicated because of complex reaction kinetics and multiscale features. Read et al.[12] provided 3D simulation information regarding an industrial scale low-density polyethylene (LDPE) autoclave reactor. Distributions of velocity, temperature, and concentration were obtained on the basis of the CFD model, and considerable deviation was observed between the CFD simulation data and ideal continuous stirred tank reactor (CSTR) results. Actual stirred tanks exhibit significant nonideal mixing. Pohn et al.[13] found that uneven mixing in heterogeneous emulsion polymerization systems significantly affects the particle size distribution of latex particles and that the established CFD-population balance model coupled model could be used to guide the scale-up of the emulsion polymerization stirred reactor. However, their work exclusively focused on studying particle coagulation in a stirred tank operated in the laminar regime and neglected the effect of agitation on latex particle size distribution. Zheng et al.[14] analyzed multizone phenomena and macromixing characteristics in industrial LDPE autoclave reactors by means of experimentation and CFD simulations and obtained prediction results well-fitted to the experimental data in a wide range of operating conditions. Moreover, the dependence of flow characteristics on impeller type was investigated in detail. However, the coupling of reaction kinetics and CFD model was not considered in their research, and, as a consequence, microscalar properties could not be predicted. Ein-Mozaffari and co-workers recently carried out simulations of polymerization system flow fields in stirred tanks by using FLUENT software.[15–17] The group simulated a solution polymerization system in a CSTR and thoroughly studied the effects of reaction temperature, monomer concentration, agitation speed, residence time, input/output location on monomer conversion, and reactor mixing performance. However, the developed isothermal laminar flow model disregarded polymerization reaction heat and several other microscale features [e.g., number-average molecular weight (M_n) and polydispersity index (PDI)] were not considered in the developed CFD model. In other words, the effect of operating conditions on the microstructure of polymer products remains unclear. More recently, Luo and co-workers[18–21] numerically simulated the multiscale properties of polymerization systems in various reactor types. The group[20,21] first developed a multiscale product model consisting of the CFD model, the population balance model, and moment equations, to characterize polypropylene formation dynamics in a catalytic fluidized bed reactor. The macro gas–solid flow field and morphological and micromolecular properties of particles were simultaneously determined in their studies. However, the simulated reactor was not a stirred reactor. To investigate the effect of operating conditions on the multiscale properties of the atom transfer radical copolymerization (ATRcoP) system in stirred vessels, Wang et al.[18,19] in Luo's group conducted several simulations. Three operating modes, namely, batch, semibatch, and continuous feeding, were investigated to study ATRcoP characteristics. Simulation results showed that each operating mode offers its own advantages and disadvantages.[18] On the basis of these results, a series of ideal CSTR models coupled with the method of moments was established. The tanks-in-series configuration is favorable in decreasing the residence time distribution and PDI. Finally, a balance between the quality and quantity of the copolymer products of the ATRcoP system was obtained.[19] However, the group only studied an ideal CSTR, and the effects of mass transfer, heat transfer, and agitation were not determined in their research.

Entire-flow field simulations in CSTRs are rare. The macroscopic flow field is known to be markedly affected by the operating conditions of the reactor (i.e., agitation speed and feeding condition). Moreover, the macroscopic flow field can influence the microscopic flow field through polymerization. Therefore, multiscale flow fields and polymerization rate are highly dependent on the reactor operating conditions. However, as described above, most previous researchers have only studied the effects of reactor structure and operating conditions on the macroscopic flow fields via the CFD technology. Limited work has focused on the relationships among operating conditions, multiscale flow fields, and polymerization. Since a CFD model can be used to describe the macroscale field and the moment method in the polymerization engineering field can be applied to characterize the microscale properties of the resultant polymers,[22,23] in the present study, a hybrid CFD model, which couples the moment method used in the polymerization engineering field into the CFD model, was established for the first time to simulate the entire flow field of living/controlled polymerization systems in CSTRs. The accuracy of the model is validated by using the available data when the stirred reactor is operated in batch mode. Considering that the impeller is one of the most important components of CSTRs, the effect of its agitation speed and structure is investigated. The effect of feeding position is then studied, and the macroscopic and microscopic flow fields are analyzed in detail. The simulation results obtained in this work provide a good reference for optimizing polymerization in CSTRs and designing the ideal microstructure of polymer products.

2. Model Development

2.1. Reaction Mechanism and Kinetic Equations

The mechanism of ATRcoP comprises initiation, propagation, transfer, and termination reactions, as shown in Table 1. Several reasonable assumptions are made in this study to simplify the reaction kinetic model according to the references.[22,24,25] The resulting reaction kinetic equations are

Table 1. Elementary reactions of ATRcoP.

Initiation	$\mathrm{RX+C \underset{k_{da,o}}{\overset{k_{a,o}}{\rightleftarrows}} R^{\bullet}+CX}$ $\mathrm{R^{\bullet}+M_A \xrightarrow{k_{in,A}} RM^{\bullet}_{A,1}}$ $\mathrm{R^{\bullet}+M_B \xrightarrow{k_{in,A}} RM^{\bullet}_{B,1}}$
Propagation	$\mathrm{RM_{A,r}X+C \underset{k_{da,A}}{\overset{k_{a,A}}{\rightleftarrows}} RM^{\bullet}_{A,r}+CX}$ $\mathrm{RM_{B,r}X+C \underset{k_{da,B}}{\overset{k_{a,B}}{\rightleftarrows}} RM^{\bullet}_{B,r}+CX}$ $\mathrm{RM^{\bullet}_{A,r}+M_A \xrightarrow{k_{p,AA}} RM^{\bullet}_{A,r+1}}$ $\mathrm{RM^{\bullet}_{A,r}+M_B \xrightarrow{k_{p,AB}} RM^{\bullet}_{B,r+1}}$ $\mathrm{RM^{\bullet}_{B,r}+M_A \xrightarrow{k_{p,BA}} RM^{\bullet}_{A,r+1}}$ $\mathrm{RM^{\bullet}_{B,r}+M_B \xrightarrow{k_{p,BB}} RM^{\bullet}_{B,r+1}}$
Transfer	$\mathrm{RM^{\bullet}_{A,r}+M_A \xrightarrow{k_{tr,AA}} RM_{A,r}+M^{\bullet}_A}$ $\mathrm{RM^{\bullet}_{A,r}+M_B \xrightarrow{k_{tr,AB}} RM_{A,r}+M^{\bullet}_B}$ $\mathrm{RM^{\bullet}_{B,r}+M_A \xrightarrow{k_{tr,BA}} RM_{B,r}+M^{\bullet}_A}$ $\mathrm{RM^{\bullet}_{B,r}+M_B \xrightarrow{k_{tr,BB}} RM_{B,r}+M^{\bullet}_B}$
Termination	$\mathrm{RM^{\bullet}_{A,r}+RM^{\bullet}_{A,s} \xrightarrow{k_{td,AA}} RM_{A,r}+RM_{A,s}}$ $\mathrm{RM^{\bullet}_{A,r}+RM^{\bullet}_{B,s} \xrightarrow{k_{td,AB}} RM_{A,r}+RM_{B,s}}$ $\mathrm{RM^{\bullet}_{B,r}+RM^{\bullet}_{B,s} \xrightarrow{k_{td,BB}} RM_{B,r}+RM_{B,s}}$ $\mathrm{RM^{\bullet}_{A,r}+RM^{\bullet}_{A,s} \xrightarrow{k_{tc,AA}} RM_{r+s}R}$ $\mathrm{RM^{\bullet}_{A,r}+RM^{\bullet}_{B,s} \xrightarrow{k_{tc,AB}} RM_{r+s}R}$ $\mathrm{RM^{\bullet}_{B,r}+RM^{\bullet}_{B,s} \xrightarrow{k_{tc,BB}} RM_{r+s}R}$

$$r_{RX}=-k_{\mathrm{a,o}}[RX][C]+k_{\mathrm{da,o}}[R^{\cdot}][CX] \tag{1}$$

$$\begin{aligned} r_{C}=&k_{\mathrm{da,o}}[R^{\cdot}][CX]-k_{\mathrm{a,o}}[RX][C]+\sum_{i}\sum_{r=1}^{\infty}k_{\mathrm{da},i}[RM^{\cdot}_{i,r}][CX]\\ &-\sum_{i}\sum_{r=1}^{\infty}k_{a,i}[RM_{i,r}X][C] \end{aligned} \tag{2}$$

$$\begin{aligned} r_{CX}=&-k_{\mathrm{da,o}}[R^{\cdot}][CX]+k_{\mathrm{a,o}}[RX][C]-\sum_{i}\sum_{r=1}^{\infty}k_{\mathrm{da},i}[RM^{\cdot}_{i,r}]\,[CX]\\ &+\sum_{i}\sum_{r=1}^{\infty}k_{a,i}[RM_{i,r}X][C] \end{aligned} \tag{3}$$

$$r_{R^{\cdot}}\ =-\sum_{i}k_{\mathrm{in},i}[M_i][R^{\cdot}]-k_{\mathrm{da,o}}[R^{\cdot}][CX]+k_{\mathrm{a,o}}[RX][C] \tag{4}$$

$$r_{M_i}=-k_{\mathrm{in},i}[R^{\cdot}][M_i]-\sum_{j}\sum_{r=1}^{\infty}(k_{\mathrm{p},ji}+k_{\mathrm{tr},ji})[RM^{\cdot}_{j,r}][M_i] \tag{5}$$

$$r_{RM_{i,r}\cdot}=\sum_{j}k_{\mathrm{p},ji}[RM_{j,r-1}\cdot][M_i]-\sum_{j}k_{\mathrm{p},ij}[RM_{i,r}\cdot][M_j]+k_{\mathrm{a},i}[RM_{i,r}X][C] \tag{6}$$

$$-k_{\mathrm{da},i}[RM_{i,r}\cdot][CX]-\sum_{j}\sum_{s=0}(k_{\mathrm{tc},ij}+k_{\mathrm{td},ij})[RM_{i,r}\cdot][RM_{j,s}\cdot]-\sum_{j}k_{\mathrm{tr},ij}[RM_{i,r}\cdot][M_j]$$

$$r_{RM_{i,r}X}=k_{\mathrm{da},i}[RM_{i,r}\cdot][CX]-k_{\mathrm{a},i}[RM_{i,r}X][C] \tag{7}$$

$$r_{RM_rR}=\frac{1}{2}\sum_{i}\sum_{j}\sum_{s=0}^{r}k_{\mathrm{tc},ij}[RM_{i,s}\cdot][RM_{j,r-s}\cdot] \tag{8}$$

$$r_{RM_r}\ =\sum_{i}\sum_{j}\sum_{s=0}^{\infty}k_{\mathrm{td},ij}[RM_{i,r}\cdot][RM_{j,s}\cdot]+\sum_{i}\sum_{j}k_{\mathrm{tr},ij}[RM_{i,r}\cdot][M_j] \tag{9}$$

In Equations (1)–(9), r_i is the reaction rate of species i, $k_{a,0}$ is activation rate constant for initiator, $k_{da,0}$ is deactivation rate constant for primary radical, $k_{a,i}$, $k_{da,i}$, $k_{in,i}$, $k_{p,ij}$, $k_{tc,ij}$, $k_{td,ij}$, $k_{tr,ij}$ is the activation rate constant, deactivation rate constant, initiation rate constant, chain propagation rate constant, combinative termination rate constant, disproportional termination rate constant, chain transfer rate constant respectively. $[M]$ is the monomer, $[RX]$ is the initiator, $[C]$ is the activator, $[CX]$ is the deactivator, $[R^{g}]$ is the primary radical, $[RM_r\cdot]$ is the propagating radical chain, $[RM_rX]$ is the dormant chain, and $[RM_r]$, $[RM_rR]$ are the dead chains with length r formed by disproportionation and coupling termination, respectively.

2.2. Microscale Model: The Method of Moments

As described above, the kinetic equations are written on the basis of the mass conservation of polymer chain length, which varies from several dozens to thousands as the operating conditions change. To solve these equations conveniently and describe the microscopic properties of polymer products, we introduce the method of moments, which is a simple deterministic method used

Macromol. React. Eng. 2016, DOI: 10.1002/mren.201600022

for modeling various polymerization processes, to rewrite reaction kinetic equations. For a generalized presentation of the method of moments, the reader is best served by referring to the works from Zhu and co-workers[22,23,26] First, several moments must be defined

$$\mu_m^i = \sum_{r=1}^{\infty} r^m [RM_{i,r}\cdot], \lambda_m^i = \sum_{r=1}^{\infty} r^m [RM_{i,r}X],$$
$$\phi_m = \sum_{r=1}^{\infty} r^m [RM_r R], \omega_m = \sum_{r=1}^{\infty} r^m [RM_r] \tag{10}$$

Here, μ_m, λ_m, ϕ_m, ω_m is the m-th moment of propagating radical, dormant chain, dead chains formed by coupling termination, dead chains formed by disproportionation termination or chain transfer to monomer respectively.

The moment equations for various species are obtained and shown in the Supporting Information (see the Supporting Information for details). The average properties of the copolymers, such as their number-average chain length (r_n), weight-average chain length (r_w), PDI, instantaneous copolymer composition (F_i), and chain-end functionality (F_t), are described as below

$$r_\mathrm{n} = \frac{\sum_i (\mu_1^i + \lambda_1^i) + \phi_1 + \omega_1}{\sum_i (\mu_0^i + \lambda_0^i) + \phi_0 + \omega_0} \tag{11}$$

$$r_w = \frac{\sum_i (\mu_2^i + \lambda_2^i) + \phi_2 + \omega_2}{\sum_i (\mu_1^i + \lambda_1^i) + \phi_1 + \omega_1} \tag{12}$$

$$\mathrm{PDI} = \frac{r_\mathrm{w}}{r_\mathrm{n}} \tag{13}$$

$$F_\mathrm{i} = \frac{k_{\mathrm{in},i}[R\cdot][M_i] + \sum_j k_{\mathrm{p},ji}\mu_0^j [M_i]}{\sum_i k_{\mathrm{in},i}[R\cdot][M_i] + \sum_i \sum_j k_{\mathrm{p},ji}\mu_0^j [M_i]} \tag{14}$$

$$F_\mathrm{t} = \frac{\sum_i \lambda_0^i}{\sum_i \mu_0^i + \sum_i \lambda_0^i + 2\phi_0 + \omega_0} \tag{15}$$

These moment equations cannot be solved independently, as they are naturally coupled with concentration and temperature. Hence, we must establish the corresponding CFD model to solve the flow fields in the reactor.

2.3. Macroscale CFD Model

The CFD models are composed of the continuity, momentum, energy, and species balance equations. In a stirred tank reactor, the Reynolds number is defined as $\mathrm{Re} = \rho N D^2/\mu$. Considering that viscosity significantly increases as the reaction progresses (0.001–10 Pa s), turbulence appears only at the beginning of the polymerization. Therefore, a laminar regime is employed in our CFD model. Similar assumption is also accepted by many other researchers.[15–17,27] The corresponding governing equations under steady state condition are shown as follows:

Continuity equation

$$\nabla\cdot(\rho\vec{v}) = 0 \tag{16}$$

where $\vec{v}$ is the velocity vector and ρ is the density of the mixture. This property is strongly dependent on temperature (T) and polymer mass fraction (w_P) and can be calculated with the correlation reported by Soliman et al.[28]

$$\rho = (1174.7 - 0.918T)(1 - w_\mathrm{P}) + (1250.0 - 0.605T)w_\mathrm{P} \tag{17}$$

Momentum equation

$$\nabla\bullet(\rho\vec{v}\vec{v}) = -\nabla p + \nabla\bullet(\overline{\overline{\tau}}) + \rho\vec{g} + \vec{F} \tag{18}$$

where in

$$\overline{\overline{\tau}} = \mu[\nabla\vec{v} + \nabla\vec{v}^T] - \frac{2}{3}\nabla\bullet\vec{v}I \tag{19}$$

In Equations (18) and (19), p is the pressure, $\overline{\overline{\tau}}$ is the stress tensor, $\vec{F}$ is external forces, $\vec{g}$ is gravitational acceleration, I is the unit tensor, μ is the viscosity of the polymerization systems. The general monomer conversion dependence of the viscosity is described as below[29]

$$\log_{10}\mu = K' + a\log_{10} X_\mathrm{m} + b\log_{10} M_\mathrm{w} \tag{20}$$

In Equation (20), a,b,K' are the coefficients used to calculate viscosity, X_m is the monomer conversion, M_w is the molecular weight of monomer.

Energy equation

Energy transfer is caused by conduction, species diffusion, and viscous dissipation. This parameter can be written as

$$\nabla\bullet(\vec{v}(\rho e + p)) = \nabla\bullet(k_\mathrm{eff}\nabla T - \sum_j h_j \vec{J_j} + (\overline{\overline{\tau_\mathrm{eff}}}\bullet\vec{v}) + S_\mathrm{h} \tag{21}$$

where,

$$e = \sum_j Y_j h_j + \frac{v^2}{2} \tag{22}$$

$$h_j = \int_{T_\mathrm{ref}}^{T} c_{\mathrm{p},j}\,\mathrm{d}T \tag{23}$$

Macromol. React. Eng. **2016**, DOI: 10.1002/mren.201600022

In Equations (21)–(23), e is the total energy, k_{eff} is the effective conductivity, $\vec{J_j}$ is the diffusion flux of species j, Y_j is the mass fraction of species j, h_j is the enthalpy of species j, T_{ref} is the reference temperature, $C_{p,j}$ is the specific heat of species j. S_h represents source term in energy equation. In the ATRcoP system, propagation reaction heat (ΔH_r), which is the only type of heat considered, is given by Equation (24) according to polymerization kinetics.

$$S_h = r_p \bullet \Delta H_r \tag{24}$$

Species balance

$$\nabla \bullet (\rho \vec{v} W_i - D_i \nabla W_i) = S_i \tag{25}$$

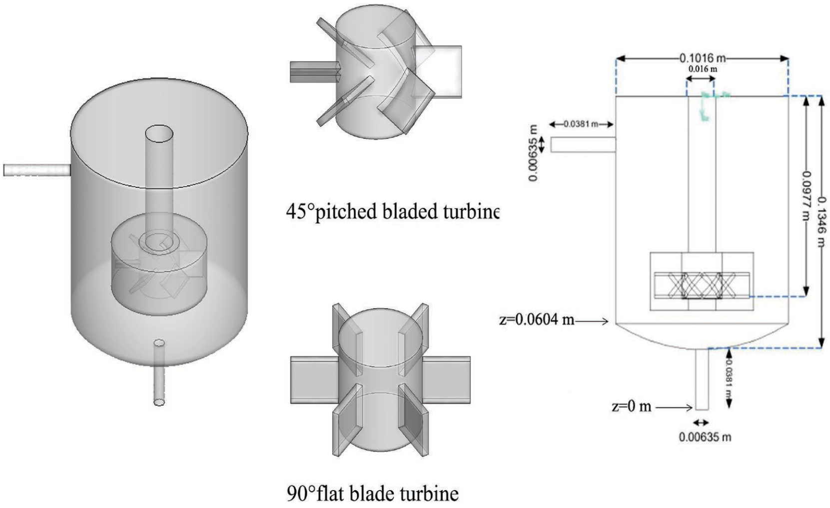

Figure 1. Geometrical features of the simulated stirred tank reactor and impellers.

In Equation (25), W_i, D_i, and S_i are the mass fraction, diffusion coefficient, and reaction source of species i, respectively.

3. Simulation Setup

All calculations are carried out in a 3D CSTR based on the simulation and experimental studies of Roudsari et al.[17] A sketch of the CSTR geometry is shown in Figure 1. The CSTR reactor consists of a round bottom cylinder with a diameter of 0.1016 and a height of 0.1346 m. No vertical baffles are placed around the tank wall. Two impeller types are applied to the reactor: a 90° flat blade turbine impeller and a 45° pitch blade turbine impeller (Figure 1). Both impellers are composed of six blades with a diameter D of 0.05 m and located with a clearance of 0.0369 m from the tank bottom. The impeller speed ranges from 60 to 600 rpm. The vessel is filled with a fluid consisting of methyl methacrylate (MMA), 2-(trimethylsilyl) ethyl methacrylate (HEMA-TMS), 2-bromoisobutyric acid ethyl ester (Eib-Br), copper(I) bromide (CuBr), copper(II) bromide ($CuBr_2$), and toluene functioning as the monomer, initiator, activator, devitalizer, and solvent, respectively. Polymers are generated as the reaction proceeds. As the chemical species are soluble in toluene, a single-phase flow model is assumed in the present study.

The commercial CFD code FLUENT 6.3.26 (Ansys Inc., USA) is employed to solve the 3D multiscale model in double-precision mode. In this mode, the ATRcoP reaction kinetic model is coupled by a user-defined function. A commercial grid generation tool, GAMBIT 2.3.16 (Ansys Inc.), is utilized to generate the 3D reactor geometries and discretize the computational domain. Considering the complexity of the reactor configuration, unstructured tetrahedral cells are used in all simulations. To verify that simulation results were not mesh dependent, simple grid sensitivity analysis were conducted based on three cases containing 103892, 188577, and 288598 cells, respectively. Simulation results of monomer conversion, M_n, and PDI changes with polymerization time were shown in Figure 2. The results indicated that a total amount of 2 88 598 cells was adequate for simulation. What's more, the grid independence test was also carried out by Roudsari et al.[17] who simulated a MMA solution polymerization system in CSTRs, which were identical to those of this work. According to their research, the final 3D model had 3 15 087 cells.

The hydrodynamics of CSTR is considerably more complicated than that of other reactors because of the rotating impellers in the former. In general, the 3D fluid domain is divided into two parts, namely, a rotating

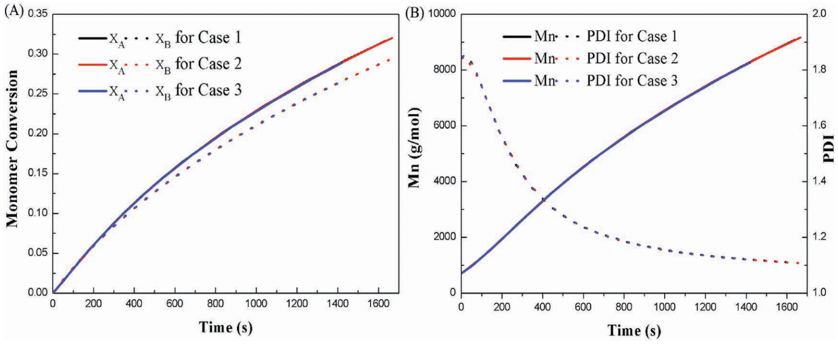

Figure 2. Grid sensitivity analysis: A) monomer conversions versus time and B) molecular weight and PDI versus time.

Table 2. Feeding conditions and boundary conditions.

Descriptions	Values
Velocity [m s^{-1}]	0.01
MMA [mol L^{-1}]	1
HEMA-TMS [mol L^{-1}]	1
Eib-Br [mol L^{-1}]	0.01
CuBr [mol L^{-1}]	0.01
$CuBr_2$ [mol L^{-1}]	5×10^{-4}
Feed temperature [K]	363.15
Operating pressure [Pa]	1 01 325
Inlet boundary condition	Velocity inlet
Outlet boundary condition	Pressure outlet
Wall boundary condition	No slip for fluid
Wall temperature [K]	363.15

domain containing the impeller and a stationary domain that includes the rest of the reactor components. In this paper, the multiple reference frame (MRF) approach was used to address impeller rotation. A reference moving zone with dimensions of $r = 0.0275$ m and $z = 0.0281$ m was created according to Roudsari et al.'s recommendations.[17] Data exchange between different fluid zones is carried out by a created grid interface, and the SIMPLE algorithm is utilized to couple pressure and velocity. A first-order upwind method (the performances of the first-order and higher-order upwind techniques are compared in the Supporting Information) is employed to discretize all terms in the CFD model. The distributions of pressure, temperature, and species mass fraction are specified prior to starting the iterative calculation. Information on the macroscale flow fields are thus obtained by solving the momentum and continuity equations. Before solving the energy equations and species equations, temperature and species for each CFD cell are transferred into the polymerization reaction kinetics equations rewritten by the method of moments. Thus, the reaction kinetics equations can be solved in each cell and the microscopic flow fields including M_n, PDI, F_i, and F_t are obtained. In addition, the reaction rates as well as the reaction heat is also obtained. Then, the energy and species balance equations, which consider the monomers, initiator, activator, and deactivator, and the moments (see the Supporting Information for more details), are solved and the distributions of temperature and species mass fraction in each cell are updated. The above process is carried out iteratively until the simulation results converge. Finally, the macroscopic and microscopic flow fields in CSTR are simulated. When the aforementioned governing equations are solved under steady-state conditions, two criteria are monitored to determine the convergence of the model: (i) the convergence precision of transport equations is less than 1×10^{-5}; and (ii) the mass fraction of unreacted monomer at the CSTR outlet does not vary with the increase in iterations. The final convergence is achieved only when the two criteria are reached. Additionally, to validate the developed CFD model, the governing equations are also solved under unsteady-state conditions (see Section 4.1). In the current study, a convergence criterion of 1×10^{-3} and an initial time step of 1×10^{-3} s with 40 iterations per time step are chosen. When the temporal iterations are converged, time step increases to 5×10^{-3} s for the purpose of saving computing time.

According to the multiscale model developed above, a number of parameters, which mainly consist of ATRcoP kinetic parameters and boundary conditions, must be provided. The reaction kinetic parameters are obtained from the references and our previous work.[18] The conditions of reaction are identical to those of the experiment listed in Table 2, and heat capacities, the heat conductivity coefficient, and the heat transfer coefficient are assumed to be constant in this study. All simulations are fed at the top of reactor, except in Subsection 4.4, "Effect of feeding position" where entire flow fields are studied in the case of the middle feeding position and bottom feeding position. The diffusion coefficients of all species in the ATRcoP system are assumed to be constant at 2.23×10^{-9} m^2 s^{-1} using the constant dilute-approximation option in FLUENT.[30] All simulations are executed in a Pentium 4 CPU running at 2.83 GHz with 4 GB of RAM.

Table 3. Comparison between the CFD simulated results and the literature data at different operating mode.

Parameters	Batch mode		Continuous mode	
	CFD simulation results	Wang et al.'s experimental data[18]	CFD simulation results	Wang et al.'s simulation results[18]
MMA%	48.15	47.79	37.98	26.45
HEMA-TMS%	38.71	37.50	35.30	24.58
M_w	33 857	33 448	18 722	8768
PDI	–	–	1.700	1.990

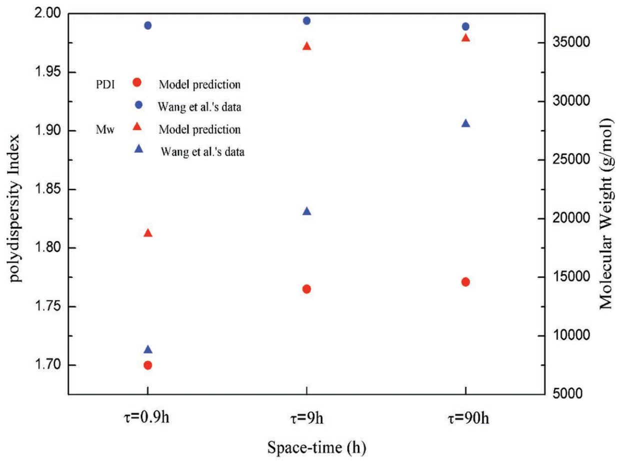

Figure 3. Comparison of the CFD simulation results of M_w and PDI with the open data at different space-time under continuous mode.

4. Results and Discussion

An original CFD model that can describe the multiscale phenomenon in 3D CSTRs was developed to achieve detailed information on entire flow fields. This section consists of four subsections. The coupled model was first verified by experimental data from our previous work, after which the validated model was applied to investigate the effect of agitation speed, impeller type, and feeding position on multiscale flow fields under steady-state conditions.

4.1. Verification of Model

To validate the developed CFD model, the comparison of the simulated results and open data in terms of monomer conversion, M_w and PDI is studied when the conditions of simulation are identical to those of the experiment listed in Table 2. The results are presented in Table 3. The simulation results of monomer conversion and weight-average molecular weight (M_w) obtained under batch mode at t = 3600 s are in good agreement with the experimental data reported by Wang et al.[18] These findings imply that the model established in the present study can be used to provide a good description of the multiscale fields of the ATRcoP system in stirred tanks.

Unfortunately, there is little experimental data for ATRcoP system in CSTR. Table 3 gives the monomer conversion, M_w and PDI comparable results when the STR is operated under continuous mode. Herein, it should be pointed out that the literature data are not experimental data but are simulation results obtained by Wang et al.[18] Obviously, our simulation results are much larger than the predicted values of the ideal mixing model obtained by them. As known to all, the production intensity of the ideal mixing reactor is the lowest under the same feeding conditions. Thus, both monomer conversion and M_w achieve higher values in the present study in comparison with those produced by an ideal CSTR. As reaction heat is taken into account in this study, an increase in reactor temperature may explain the high conversion observed.

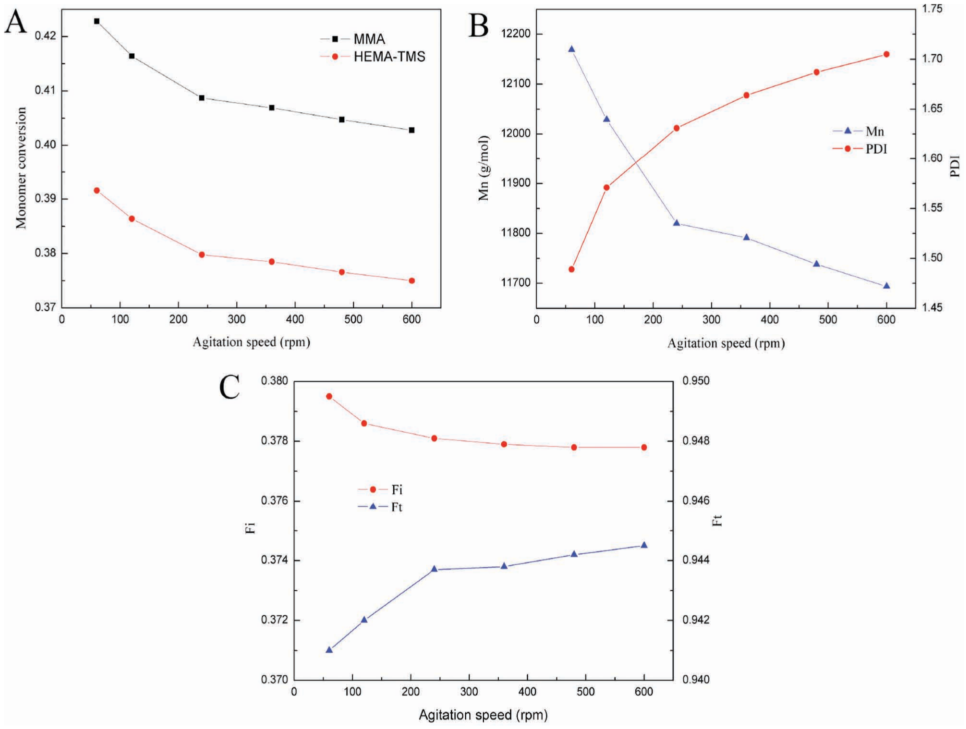

Figure 4. Simulation results of monomer conversion, M_n, PDI, Fi, and Ft at the outlet of reactor versus agitation speed.

Macromol. React. Eng. 2016, DOI: 10.1002/mren.201600022

Higher PDI values are mainly attributed to the development of a wider residence time distribution under perfect mixing conditions.

When the stirred reactor is operated in continuous mode, similar PDI prediction results (Figure 3) are observed under different space times (τ), which represents a central parameter denoting the ratio of reactor volume and volumetric feed flow often used in the design of chemical reactors. PDI shows slight increases as τ increases. By contrast, M_w changes substantially as τ increases from 0.9 to 90 h. At lower τ, the polymerization cannot be completed because of short-circuiting of the unreacted monomer. Thus, M_w may initially be observed to increase rapidly with increase in τ. Further increases in τ promote slower chain propagation reaction rates as the monomer concentration is maintained at low levels. Therefore, M_w tends to increase gradually. Coincidentally, a similar M_w trend was predicted by Wang et al.,[18] who simulated M_w and PDI in CSTR at different space times.

In summary, the established model suitably describes an actual STR, as the simulation results are in fairly good agreement with experimental data under batch mode. Certain additional flow field information can also be obtained in the present model when compared with the perfect mixing model. In actual reactors, flow fields are usually complicated and change with the operation conditions, especially during agitation of STRs. The following three subsections will investigate the effect of impeller speed, impeller type, and feeding position on multiscale flow fields in CSTRs.

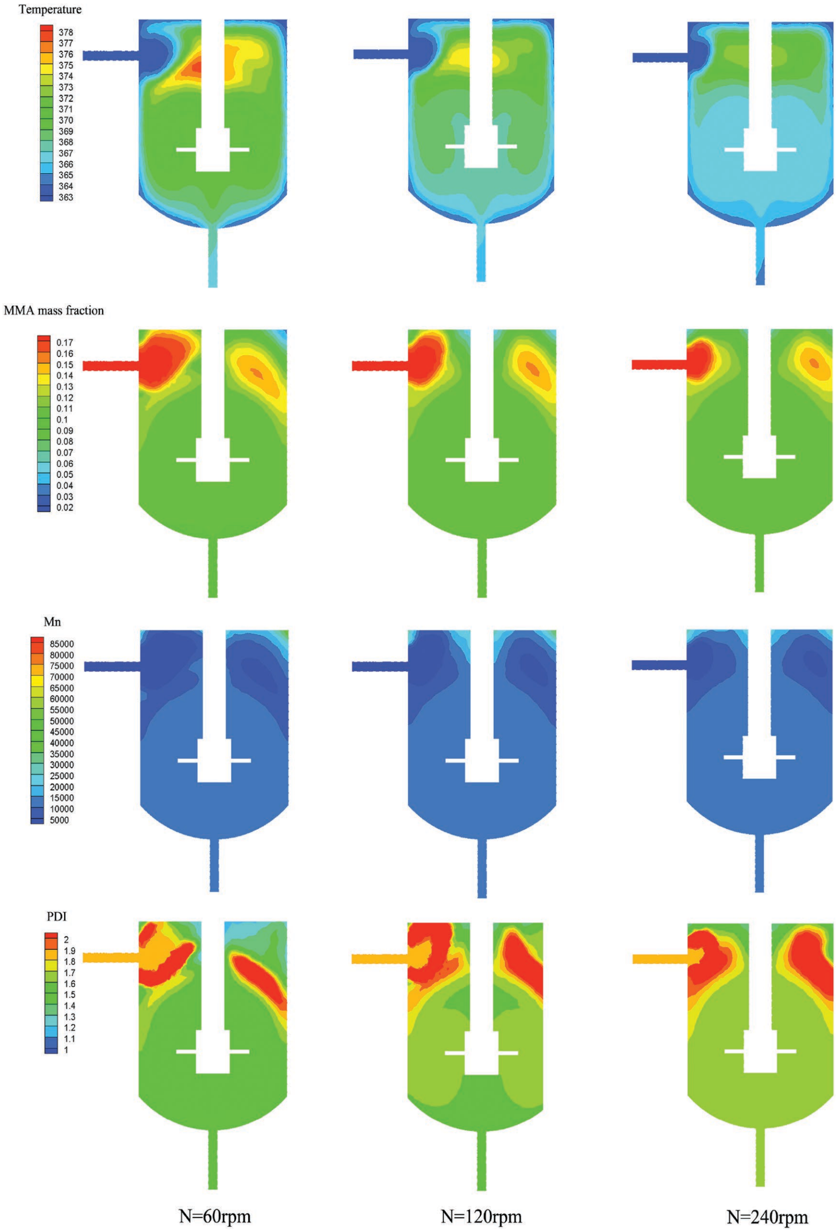

Figure 5. The contours of temperature, MMA mass fraction, M_n, and PDI at different agitation speed.

4.2. Effect of Impeller Speed

Impeller speed performs a significant function in improving CSTR flow fields. Several simulations were carried out in this section to investigate the effect of impeller speed on CSTR performance. Figure 4 depicts the evolution of monomer conversion, M_n, PDI, F_i, and F_t (those are obtained by surface average, the same below) at the reactor outlet as the agitation speed is varied from 60 to 600 rpm. As can be seen from Figure 4A, monomer conversion gradually decreases with increasing impeller speed. Short-circuiting of unreacted monomer at higher agitation speeds may be a crucial mechanism affecting polymer production.[17] As mentioned above, two types of ideal flow conditions, namely, plug flow and perfect mixing, are involved in reactors, and the flow pattern in an actual reactor usually falls in between these two flow conditions. With increases in stirring speed, the flow pattern in the reactor approaches perfect mixing, thereby leading to a decrease in monomer conversion, which can explain the decreased M_n [Figure 4B]. PDI increases at higher agitation speeds may be due to the development of a broad residence time distribution. Figure 4C shows the plots of copolymer composition and chain-end functionality at the reactor outlet versus agitation speed. In the case of a constant monomer feeding ratio (1:1), the instantaneous composition of MMA remains at about 37.8%, and no significant gradient in composition is found. Furthermore, the chain-end functionality of the copolymer exceeds 94%, thus indicating that the ATRcoP system involves living polymerization.

Figure 5 shows the CFD contours of temperature, MMA mass fraction, M_n, and PDI under the same inlet conditions with three different agitation speeds of 60, 120, and 240 rpm. Evidently, macroscopic flow field in the stirred tank becomes increasingly even with increases in stirring speed. The temperature distributions reveal that hotspots shrink because of increases in convection heat transfer rate with increasing agitation speed. From Figure 5, a large amount of unreacted monomers is present in the upper regions away from the impeller at $N = 60$ rpm. In other words, stagnant zones easily form at lower agitation speeds. With increasing agitation speed, however, the distribution of the monomer mass fraction changes considerably, and dead zones nearly completely disappear at $N = 240$ rpm. Temperature and concentration distributions are known to directly determine reaction rate, which may affect the microstructure of polymer products. As previously described, fluid flow closely approximates perfect mixing as the stirring speed increases. Therefore, M_n decreases with increasing agitation speed, whereas PDI shows an increasing trend. PDI is relatively small in the

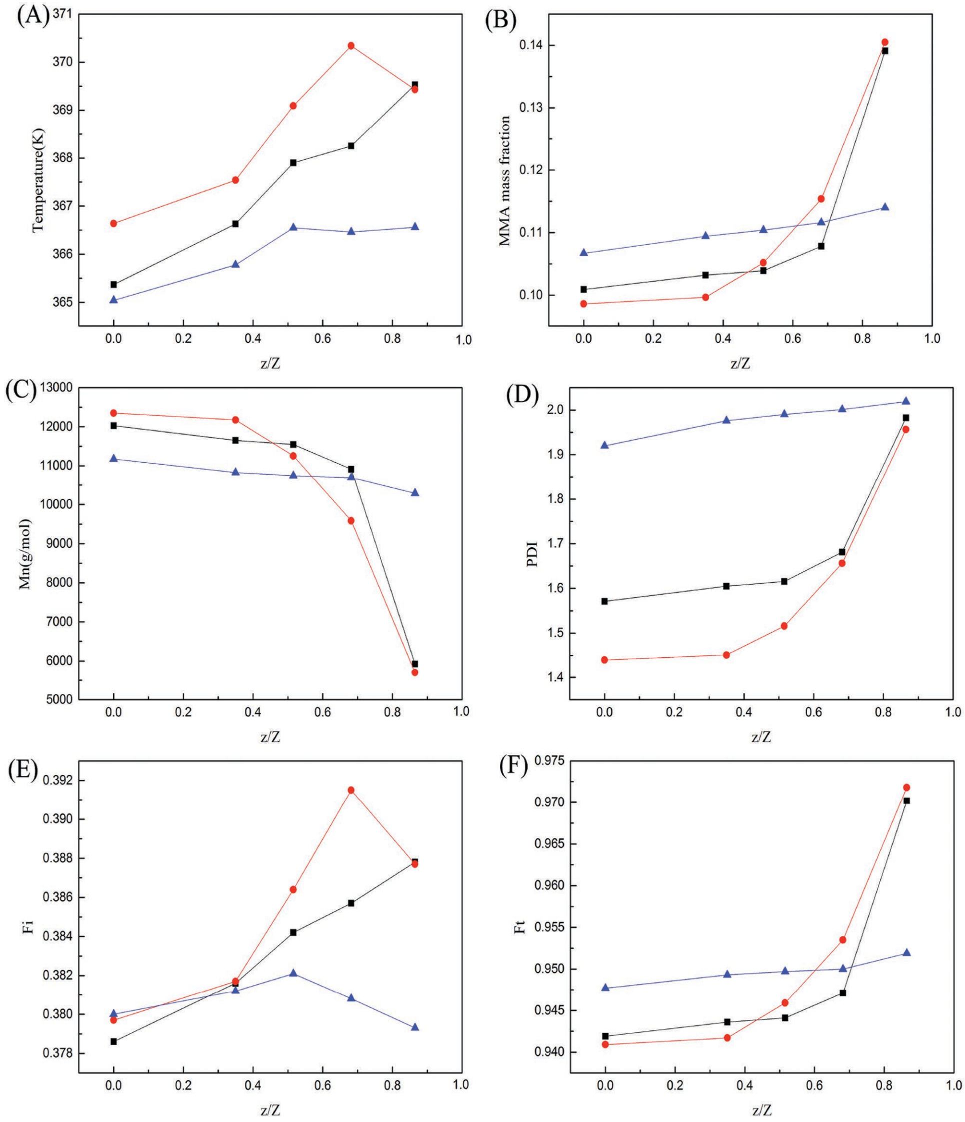

Figure 6. The axial direction distribution of A) temperature, B) MMA mass fraction, C) M_n, D) PDI, E) F_i, and F) F_t for three different impeller types: ● 90° flat blade turbine, ■ 45° pitched impeller, ▲ multiple impeller.

Macromol. React. Eng. **2016**, DOI: 10.1002/mren.201600022

vicinity of the impeller at a low impeller speed of 60 rpm but increases considerably, even exceeding 2, at regions away from the impeller. These differences further increase with increasing impeller speed, possibly because the broad residence time distribution at higher agitation speeds and mixing of fluid particles with different residence times directly lead to PDI increases.

In summary, stirring speed observably affects the multiscale flow fields in the vessel, and an appropriate speed is key to control the polymer microstructure. The cases simulated above indicate that ATRcoP shows good controllability at lower impeller speeds. Therefore, unless otherwise stated, $N = 120$ rpm was applied in subsequent simulations. The simulation results also show the importance of agitation in stirred reactors.

4.3. Effect of Impeller Types

Figure 6 displays the axial direction distributions of T, MMA mass fraction, M_n, PDI, F_i, and F_t, those are obtained by surface average at different z. The effect of three impeller types on flow fields was compared. As can be seen from Figure 6A, the temperature distribution basically shows a decreasing trend along the axial direction from the top to the bottom of the stirred tank because higher reactant concentrations at the inlet position lead to faster polymerization reaction rates and the consequent release of a considerable amount of reaction heat. The feeding position is located away from impeller. Because of the low level of disturbance induced by the impeller, low convective heat transfer rates are observed and the temperature is higher at the reactor inlet than at other locations. The impeller configuration significantly affects the temperature distribution in the reactor. For a single impeller structure, the six-bladed 45°-pitched impeller configuration can effectively promote axial and radial mixing of the fluid, and the mixing efficiency afforded by the configuration is superior to that of the six-bladed, 90° flat blade turbine. The dual stage configuration with the six-bladed 45°-pitched impeller exhibits the highest mixing efficiency among the three impeller types studied. The temperature distribution becomes uniform and the maximum temperature difference is ≈1 K only in the reactor with multiple impellers. The MMA mass fraction shows a similar distribution trend [Figure 6B]. The distributions of temperature and reactant concentration depend strongly on mixing. Higher mixing efficiency of the impeller translates to more uniform reactant distributions or higher outlet concentrations. This finding further confirms the mixing efficiency of each impeller.

The axial distribution of M_n is given in Figure 6C. We can see that the impeller configuration significantly affects M_n. The dual-stage impeller promotes uniformity of the temperature and concentration distributions [Figures 6A,B] and can thus be used to control the polymerization reaction rate. This advantage, however, is offered at the expense of reactor production intensity. M_n decreases as the mixing efficiency of the impeller increases under the same operating conditions. PDI is considerably affected by the residence time distribution, which is correlated with the impeller type. The residence time distribution broadens when the dual-stage impeller is used, and the PDI exceeds 1.90. By contrast, with the six-bladed 90° flat blade turbine, PDI appears higher only at the reactor inlet and is ≈1.45 at the reactor outlet [Figure 6D]. Thus, CSTRs are often coupled in a series, usually with a maximum of three setups, to form a reactor

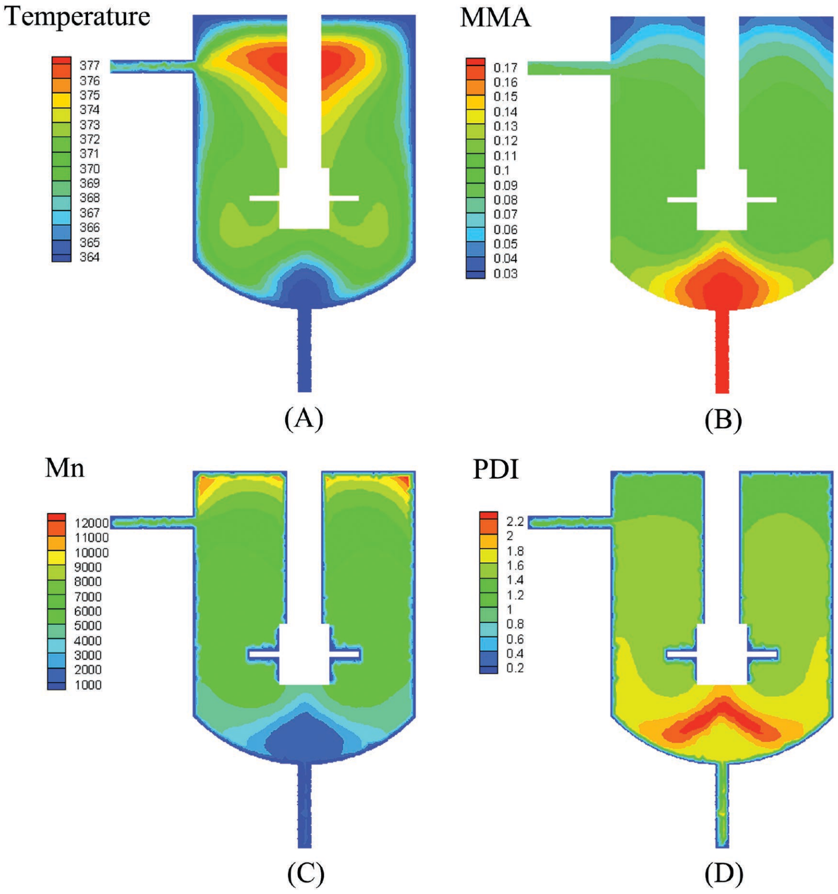

Figure 7. The contours of A) temperature, B) MMA mass fraction, C) M_n, and D) PDI under bottom feeding mode.

cascade.[31] Figure 6E,F describes the distributions of copolymer composition and chain-end functionality. No significant gradient in composition is found under different impeller configurations, and the copolymer composition is considered to be mainly controlled by the monomer ratio. Chain-end functionality is greater than 0.94 in all simulations [Figure 6F], as discussed in Section 4.2.

In summary, differences in mixing efficiency among the three impeller types are reflected by the distribution of macroscopic and microscopic flow fields. The single-stage impeller could ensure a narrow residence time distribution, which is key for preparing single dispersion polymer products. By contrast, the dual-stage impeller can effectively improve temperature and concentration distributions in the reactor, which is conducive to polymerization rate control. We can see from previous simulation results that mixing at the feeding position is usually poor at high PDIs. Feeding position optimization appears to be an important strategy to improve reactor performance.

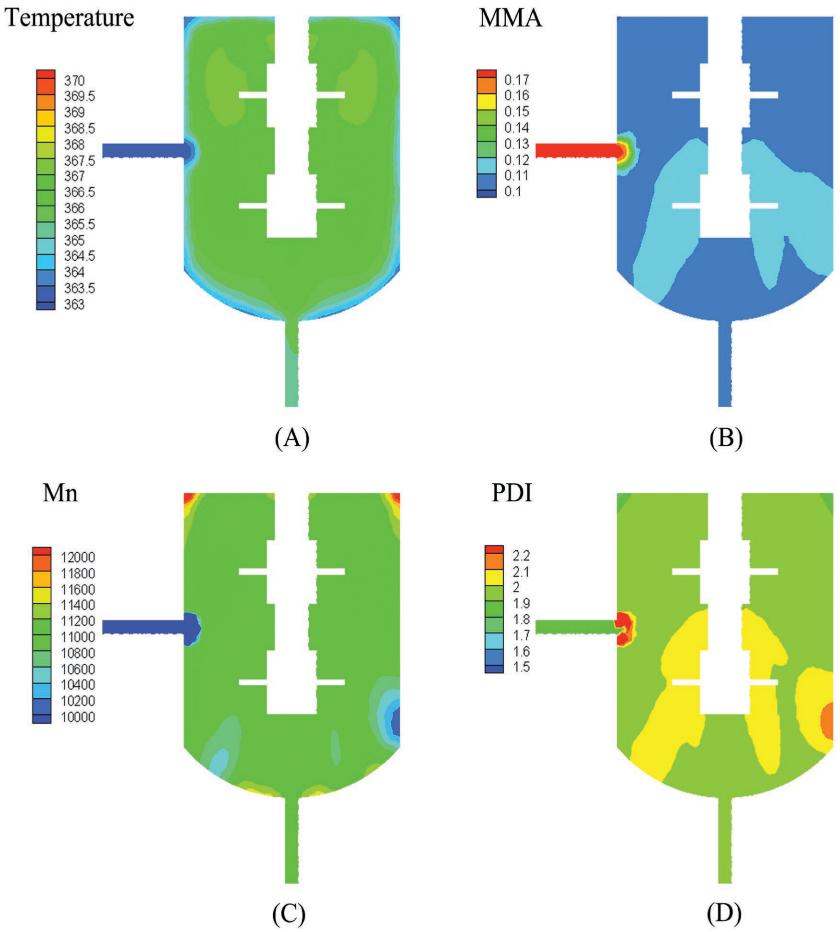

Figure 8. The contours of A) temperature, B) MMA mass fraction, C) M_n, and D) PDI under middle feeding mode.

4.4. Effect of Feeding Position

The raw material feeding position is one of the most important parameters affecting reactor design. It is a common practice in industry to feed the reactants from the bottom of continuous reactor in order to secure a full-tank operation and well mixing. Saeed and Ein-Mozaffari[32] pointed out that input/output locations are responsible for the development of nonideal flow characteristics, such as channeling and dead zones. Patel et al.[15] achieved a high degree of homogeneity at a low agitation speed when the feed is placed at the reactor bottom. The top feeding mode has been investigated in Section 4.3, where poor reactant mixture has been observed near the feeding position. In this section, our attention was mainly focused on the effect of bottom feeding mode with single-stage impeller and middle feeding mode with dual-stage impeller on the multiscale flow fields.

Figure 7 shows the multiscale flow fields under the bottom feeding mode with the agitation speed of 120 rpm. As can be seen, mixing quality has been improved when compared with those of the top feeding mode, thus making the ATRcoP enhanced. However, the hotspots still exist away from the impeller [see Figure 7A].

What's more, the middle feeding mode, wherein the feeding position is located between the impellers (Figure 8), was employed to study entire flow fields in stirred tank reactors. The contours of temperature, MMA mass fraction, M_n, and PDI are shown in Figure 8. As can be seen from Figure 8A, the stirred tank achieves an approximately isothermal distribution, and the hotspots completely disappear. The middle feeding mode promotes considerably improved MMA monomer mass fraction distribution [Figure 8B]. The MMA mass fraction shows even distribution immediately after feeding into the reactor and is maintained at ≈11% throughout the reactor. Figure 8C shows the relatively uniform distribution of M_n. However, a dead zone remains at the corner of the reactor. A previous study reported that the baffle is an effective device to eliminate dead zones in stirred tank reactors.[33] The middle feeding mode effectively improves flow field distribution, and the polymer PDI at the reactor outlet cross-section was ≈1.966 [Figure 8D]. This value closely approaches the PDI value of perfect mixing model under the same inlet operation condition. To obtain

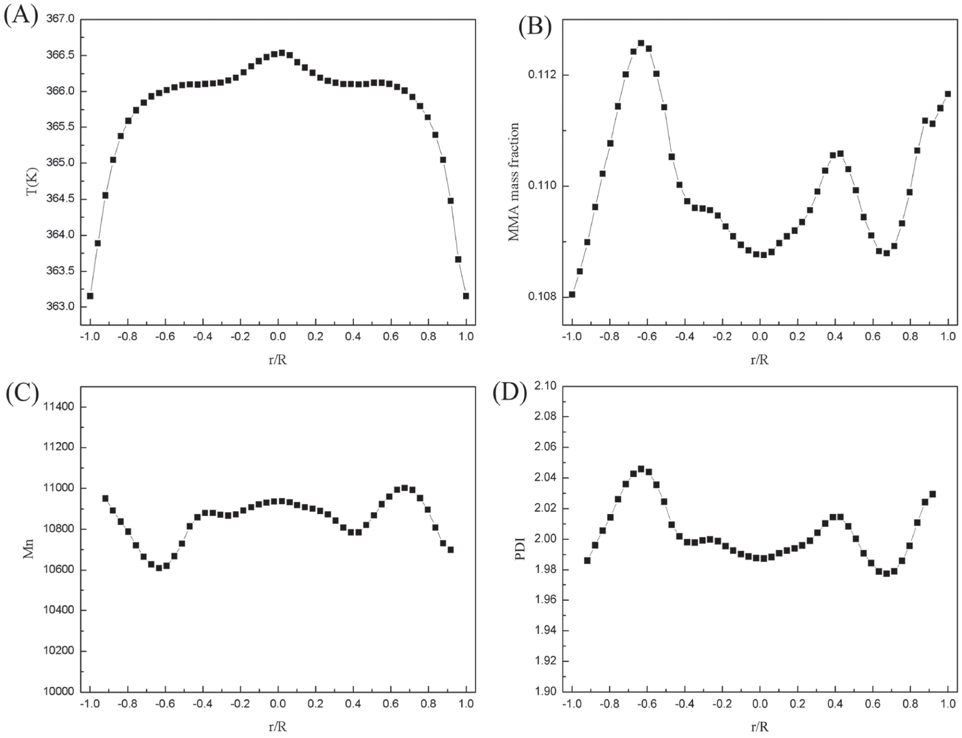

Figure 9. The radial distribution profiles of A) temperature, B) MMA mass fraction, C) M_n, and D) PDI at z = 0.0604 m.

more detailed flow field information on stirred reactors, we studied the radial distribution of several important parameters at z = 0.0604 m (Figure 9). Figure 9A shows the reactor radial temperature distribution, which is basically maintained at 366 K. A large temperature gradient is exclusively observed near the reactor wall. Compared with the symmetrical temperature distribution, the MMA mass fraction distribution is more easily affected by the impeller [Figure 9B]. The MMA mass fraction is roughly stable at 11%, and differences in radial distribution are not apparent (<0.4%). Similarly, the distributions of M_n and PDI are nearly uniform in the radial direction. Viscosity increases sharply as polymerization proceeds, and polymer accumulation or "wall-fouling," which results in a large M_n near the reactor wall, appears. In the present study, however, the axial and radial distributions of M_n are nearly uniform, and the sticky wall phenomenon of the polymer is not observed [Figure 9C]. PDI may exceed 2 at certain local positions in the middle feeding mode [Figure 9D].

5. Conclusion

In this work, a CFD model coupled with the moment method is developed to simulate the ATRcoP system of MMA and HEMA-TMS in a 3D CSTR. To validate the developed CFD model, comparison of the simulation results with experimental data in terms of monomer conversion, M_w, and PDI was carried out as the stirred reactor was operated in different modes. The simulation results were in fairly good agreement with the experimental data in batch mode. Certain additional flow field information can also be obtained in the present model when compared with the predicted results of the ideal CSTR model. Particular attention was focused on studying agitation in CSTRs by the MRF approach, and multiscalar properties were characterized by macroscopic mixing fields and the microscopic structures of the resultant polymer.

On the basis of the validated models, we first investigated several important parameters at the reactor outlet at different agitation speeds. Monomer conversion and M_n gradually decreased with increasing impeller speed. The PDI increase observed at higher agitation speeds may be due to the development of a broader residence time distribution. The instantaneous composition of MMA remained at about 37.8%, and a significant composition gradient was not found. These findings imply that the composition gradient is spontaneous and uncontrollable. Furthermore, the chain-end functionality of the copolymer exceeded 94%, which indicates that the ATRcoP system involves living polymerization. Hotspots and dead zones nearly completely disappeared at higher agitation speeds.

We then numerically studied the effects of different impeller types on flow fields. We found that a single-stage impeller could ensure a narrow residence time distribution, which is key for preparing single dispersion polymer products, whereas a dual-stage impeller can effectively improve temperature and concentration distribution, which is conducive to polymerization rate control. Finally, the middle feeding mode and bottom feeding mode were employed to study entire flow fields in CSTR. The middle feeding mode effectively improved reactant and temperature distributions and promoted uniformity of the radial temperature, MMA mass fraction, M_n, and PDI distributions.

The current work describes multiscale fields in CSTR. The simulation results highlight the importance of stirring and provide useful guidelines for the scale-up of stirred-tank polymerization reactors and preparing single dispersion polymer products.

Supporting Information

Supporting Information is available from the Wiley Online Library or from the author.

Acknowledgements: The authors thank the National Ministry of Science and Technology of China (Grant No. 2012CB21500402) and the National Natural Science Foundation of China (Grant Nos. U1462101 and 21476267) for supporting this work.

Received: April 27, 2016; Published online: ; DOI: 10.1002/mren.201600022

Keywords: ATRcoP; CFD; mathematical modeling; mixing; stirred-tank reactor

[1] T. Kumaresan, N. K. Nere, J. B. Joshi, *Ind. Eng. Chem. Res.* **2005**, *44*, 9951.
[2] R. Zadghaffari, J. S. Moghaddas, J. Revstedt, *Comput. Chem. Eng.* **2009**, *33*, 1240.
[3] Y. Y. Bao, J. Yang, L. Chen, Z. M. Gao, *Ind. Eng. Chem. Res.* **2012**, *51*, 12411.
[4] M. Sommerfeld, S. Decker, *Chem. Eng. Technol.* **2004**, *27*, 215.
[5] H. N. Wang, X. Q. Jia, X. Wang, Z. X. Zhou, J. P. Wen, J. L. Zhang, *Appl. Math. Model.* **2014**, *38*, 63.
[6] B. N. Murthy, R. S. Ghadge, J. B. Joshi, *Chem. Eng. Sci.* **2007**, *62*, 7184.
[7] M. H. Vakili, M. N. Esfahany, *Chem. Eng. Sci.* **2009**, *64*, 351.
[8] T. Dyakowski, R. A. Williams, *Powder Technol.* **1993**, *77*, 135.
[9] A. R. Khopkar, J. Aubin, C. Xuereb, N. L. Sauze, J. Bertrand, V. V. Ranade, *Ind. Eng. Chem. Res.* **2003**, *42*, 5318.
[10] J. D. Wilde, G. V. Engelandt, G. J. Heynderickx, G. B. Marin, *Powder Technol.* **2005**, *151*, 96.
[11] V. S. Sutkar, N. G. Deen, V. Salikov, S. Antonyuk, S. Heinrich, J. A. M. Kuipers, *Powder Technol.* **2015**, *270*, 537.
[12] N. K. Read, S. X. Zhang, W. H. Ray, *AIChE J.* **1997**, *43*, 104.
[13] J. Pohn, M. Heniche, L. Fradette, M. Cunningham, T. McKenna, *Macromol. Symp.* **2011**, *302*, 133.
[14] H. J. Zheng, Z. L. Huang, Z. W. Liao, J. D. Wang, Y. R. Yang, Y. L. Wang, *Ind. Eng. Chem. Res.* **2014**, *53*, 14865.
[15] H. Patel, F. Ein-Mozaffari, R. Dhib, *Comput. Chem. Eng.* **2010**, *34*, 421.
[16] H. Patel, F. Ein-Mozaffari, R. Dhib, *Chem. Eng. Technol.* **2010**, *33*, 258.
[17] S. F. Roudsari, F. Ein-Mozaffari, R. Dhib, *Chem. Eng. J.* **2013**, *219*, 429.
[18] W. Wang, Y. N. Zhou, Z. H. Luo, *Ind. Eng. Chem. Res.* **2014**, *53*, 11873.
[19] W. Wang, Y. N. Zhou, L. Shi, Z. H. Luo, *Polym. Eng. Sci.* **2015**, *55*, 1030.
[20] Y. P. Zhu, G. Q. Chen, Z. H. Luo, *Macromol. React. Eng.* **2014**, *8*, 609.
[21] Y. P. Zhu, Z. H. Luo, J. Xiao, *Comput. Chem. Eng.* **2014**, *71*, 39.
[22] S. P. Zhu, *Macromol. Theor. Simul.* **1999**, *8*, 29.
[23] S. P. Zhu, *J. Polym. Sci. Polym. Phys.* **1999**, *37*, 2692.
[24] R. Wang, Y. W. Luo, B. G. Li, S. P. Zhu, *AIChE J.* **2007**, *53*, 174.
[25] Y. N. Zhou, J. J. Li, Z. H. Luo, *J. Polym. Sci. Polym. Chem.* **2012**, *50*, 3052.
[26] R. Wang, Y. W. Luo, B. G. Li, X. Y. Sun, S. P. Zhu, *Macromol. Theor. Simul.* **2006**, *15*, 356.
[27] Z. G. Meszéna, A. F. Johnson, *Macromol. Theory Simul.* **2001**, *10*, 123.
[28] M. A. Soliman, T. Aljarboa, M. Alahmad, *Polym. Eng. Sci.* **1994**, *34*, 1464.
[29] J. S. Sangwai, D. N. Saraf, S. K. Gupta, *Polymer* **2006**, *47*, 3028.
[30] R. A. Waggoner, F. D. Blum, J. M. D. Macelroy, *Macromolecules* **1993**, *26*, 6841.
[31] T. O. Salmi, J. P. Mikkola, J. P. Warna, *Chemical reaction engineering and reactor technology*, Boca Raton: CRC Press, **2011**.
[32] S. Saeed, F. Ein-Mozaffari, *J. Chem. Technol. Biotechnol.* **2008**, *83*, 559.
[33] C. Xuereb, J. Bertrand, *Chem. Eng. Sci.* **1996**, *51*, 1725.